

# Extreme Sensitivity of the YORP Effect to Small-Scale Topography

Thomas S. Statler

*Astrophysical Institute, Department of Physics and Astronomy, 251B Clippinger Research Laboratories, Ohio University, Athens, OH 45701, USA*

---

## Abstract

Radiation recoil (YORP) torques are shown to be extremely sensitive to small-scale surface topography, using numerical simulations. Starting from a set of “base objects” representative of the near-Earth object population, random realizations of three types of small-scale topography are added: Gaussian surface fluctuations, craters, and boulders. For each, the expected relative errors in the spin and obliquity components of the YORP torque caused by the observationally unresolved small-scale topography are computed. Gaussian power, at angular scales below an observational limit, produces expected errors of order 100% if observations constrain the surface to a spherical harmonic order  $l \lesssim 10$ . For errors under 10%, the surface must be constrained to at least  $l = 20$ . A single crater with diameter roughly half the object’s mean radius, placed at random locations, results in expected errors of several tens of percent. The errors scale with crater diameter  $D$  as  $D^2$  for  $D > 0.3$  and as  $D^3$  for  $D < 0.3$  mean radii. Objects that are identical except for the location of a single large crater can differ by factors of several in YORP torque, while being photometrically indistinguishable at the level of hundredths of a magnitude. Boulders placed randomly on identical base objects create torque errors roughly 3 times larger than do craters of the same diameter, with errors scaling as the square of the boulder diameter. A single boulder comparable to Yoshinodai on 25143 Itokawa, moved by as little as twice its own diameter, can alter the magnitude of the torque by factors of several, and change the sign of its spin component at all obliquities. Most of the total torque error produced by multiple unresolved craters is contributed by the handful of largest craters; but both large and small boulders contribute comparably to the total boulder-induced error. A YORP torque prediction derived from groundbased data can be expected to be in error by of order 100% due to unresolved topography. Small surface changes caused by slow spin-up or spin-down may have significant stochastic effects on the spin evolution of small bodies. For rotation periods between roughly 2 and 10 hours, these unpredictable changes may reverse the sign of the YORP torque. Objects in this spin regime may random-walk up and down in spin rate before the rubble-pile limit is exceeded and fissioning or loss of surface objects occurs. Similar behavior may be expected at rotation rates approaching the limiting values for tensile-strength dominated objects.

*Key words:* ASTEROIDS, DYNAMICS, ASTEROIDS, ROTATION, ASTEROIDS, SURFACES, NEAR-EARTH OBJECTS

---

## 1. Introduction

Radiation-recoil effects are now understood to be major drivers in the evolution of small bodies in the Solar System. The secular drift in orbital elements produced by the Yarkovsky effect is a dominant mechanism in the spread of asteroid families (Bottke et al., 2001) and in the replenishment of the near Earth object (NEO) population from the inner main belt (Bottke et al., 2002). Torques produced by the YORP effect can compete with, and even dominate, collisional and tidal torques on main belt asteroids and NEOs smaller than a few km in diameter (Rubincam, 2000; Bottke et al., 2006, and references therein).

Recent observational efforts have achieved direct detection of the influence of the Yarkovsky and YORP mechanisms. Radar observations of 6489 Golevka show non-gravitational accelerations consistent with Yarkovsky predictions (Chesley et al., 2003). Photometric observations of 1862 Apollo (Kaasalainen et al., 2007) and 1620 Geographos (Ďurech et al., 2008a), and photometric and radar observations of (54509) 2000 PH<sub>5</sub> (subsequently named

---

*Email addresses:* statler@ohio.edu (Thomas S. Statler)

YORP) (Lowry et al., 2007; Taylor et al., 2007) indicate accelerations in spin rate consistent with YORP models and not attributable to tidal torques. However, the YORP models contain substantial systematic uncertainties, because the objects' shapes and surface properties are not sufficiently constrained by observations. In the case of 1862 Apollo, models computed by Kaasalainen (2004) with slightly different rotation pole positions and shapes span a range of  $\sim \pm 25\%$  around the measured acceleration. For 54509 YORP, the models computed by Taylor et al. (2007), using a range of shapes and surface roughnesses, span a factor of  $\sim 3$  in predicted acceleration; and, in fact, they all systematically overestimate the observed effect, by factors of 2 to 7.<sup>1</sup> Considering the extensive observational effort devoted to these objects, the ambiguity in the results raises considerable concern as to whether YORP predictions derived from groundbased light curve and/or radar data can ever be sufficiently precise to permit quantitative tests of the theory.

This concern is only deepened by the history of YORP calculations made for 25143 Itokawa before and after the arrival of the Hayabusa spacecraft. Using pre-encounter shape models derived from radar observations (Ostro et al., 2004) and photometric light curves (Kaasalainen et al., 2003), Vokrouhlický et al. (2004) predicted a rotational acceleration of roughly half a part in  $10^4$  per year, with an estimated uncertainty of  $\pm 30\%$ . Scheeres et al. (2007) subsequently recomputed the YORP prediction, first from a similar pre-encounter model (Gaskell et al., 2006), obtaining a result consistent with that of Vokrouhlický et al. (2004), and then from a sequence of shape models of progressively higher resolution based on *in situ* Hayabusa data. The first post-encounter shape model was found to imply a rotational deceleration, meaning that pre-encounter models had been unable to correctly predict even the sign of the effect. Subsequent models incorporating the later Hayabusa data resulted in YORP accelerations that did not converge as the resolution increased. Scheeres et al. (2007) conclude that, even at sub-meter resolution, the essential geometry of the interaction between the surface and the incoming and outgoing radiation is not adequately represented. In the past year the situation has become even murkier. Scheeres and Gaskell (2008) show that the torque on 25143 Itokawa is very sensitive to the position of the center of mass; and the predicted acceleration has still not been detected (Durech et al., 2008b).

The foregoing stories motivate this paper, which asks whether extreme sensitivity to small-scale surface topography is a characteristic of the YORP effect itself, or is limited to a comparatively small number of unfortunately shaped objects. This question has pragmatic as well as predictive consequences. First, dynamically significant small scale topography may be observationally unresolvable. I will show below that, indeed, neglecting topographic features, such as moderate sized craters, that are indistinguishable from the ground can lead to errors in YORP predictions of order unity. As a result, shape models derived from groundbased data are unlikely ever to yield precise predictions of YORP torques. Second, dynamically significant small scale topography may, in some situations, be unpredictably changeable. I will demonstrate that a small displacement of a single large boulder can, in the right circumstances, completely reverse the sign of the YORP torque. This implies that a YORP cycle (Rubincam, 2000) can be interrupted in a major way by a comparatively minor event, and suggests that the spin evolution of small NEOs may be more stochastic than previously recognized.

The theoretical foundations and basic behavior of the YORP effect have been analyzed extensively by analytic, semi-analytic, and numerical means (e.g., Scheeres, 2007b; Nesvorný and Vokrouhlický, 2007, 2008; Breiter and Michalska, 2008; Micheli and Paolicchi, 2008; Mysen, 2008b,a). These works have elucidated how asymmetries in the illuminated and radiating surface couple to produce the now familiar behavior of the orbit-averaged torque components as a function of obliquity (Vokrouhlický and Čapek, 2002), and have provided strategies for computing torques for realistic asteroid models. This paper adopts a purely numerical treatment, analyzing a large number of simulated objects to yield statistically meaningful results in the nonlinear regime where shadowing is important.

The remainder of the paper is laid out as follows. In Section 2, I describe the calculation of YORP torques for simulated asteroids. I define a set of “base objects” on which the effect of small-scale topography will be tested, and describe how topography is added to the objects, in the form of Gaussian surface fluctuations, craters, or boulders. In Section 3, I demonstrate that small scale topography, at a level difficult or impossible to constrain from groundbased observations, can typically be expected to alter YORP torques by tens of percent or more. In particular, the magnitude, and even the sign, of the torque can hinge on the location of a single large crater or boulder. In Section 4, I discuss the implications of these results, both for accurate predictions of the YORP effect and for the YORP-driven evolution of small NEOs.

---

<sup>1</sup>Scaling down the models by these factors was necessary to achieve the excellent fit in Fig. 2 of Lowry et al. (2007), as explained in the caption to that figure.

## 2. Method

### 2.1. Calculation of Torques

Radiation interacting with the surface of a body can impart a torque through the momentum it carries. It is conceptually helpful to split the interaction into three parts: (1) the momentum deposited on the surface by arriving photons; (2) the recoil imparted to the surface by departing reflected photons; and (3) the recoil imparted by departing reradiated photons. In this paper I focus specifically on the third contribution, the reradiation torque. The first contribution can be shown to cancel identically when averaged around an orbit (Nesvorný and Vokrouhlický, 2008). The second is proportional to the albedo, and becomes insignificant for a sufficiently dark surface; and, as Nesvorný and Vokrouhlický (2007) point out, if the reflected and reradiated intensities are both assumed isotropic, then the torque contributions are parallel.

I compute the torques on simulated objects using the TACO<sup>2</sup> code, developed by the author and students at Ohio University. The object’s surface is represented using a standard triangular tiling (Lagerros, 1996). For all results presented here, 6,394 vertices and 12,784 tiles are used, for an average angular resolution of approximately 7.5° (3 tiles wide). For comparison, typical shape models derived from asteroid light curve observations have 1,000 to 2,000 vertices and 2,000 to 4,000 tiles (e.g., Āurech et al., 2007). Models obtained from radar observations and currently archived in the Planetary Data System (PDS) have typically around 4,000 vertices and 8,000 tiles. Using groundbased data alone, currently only 4 objects (1620 Geographos, 25143 Itokawa, 4179 Toutatis, and 52760) have been modeled at resolutions equal to or finer than that used in this paper.

A horizon map (the maximum elevation  $\psi_h$  of all visible parts of the surface as a function of azimuth  $\eta$ , measured relative to local west) is computed at the centroid of each tile when the surface is initially defined. Shadowing is handled by requiring that the Sun not be blocked by other parts of the surface for the tile to be illuminated. An illuminated tile absorbs a flux  $F_{\text{abs}}$  given by

$$F_{\text{abs}} = F\mu_0 [1 - r_{\text{hem}}(\mu_0)], \quad (1)$$

where  $F$  is the incident flux,  $\mu_0$  is the cosine of the angle between the incident flux and the surface normal, and  $r_{\text{hem}}$  is the directional-hemispheric reflectance or hemispheric albedo. TACO computes  $r_{\text{hem}}$  using eq. (42) of Hapke (2002), assuming a single Henyey-Greenstein phase function. For definiteness I adopt the mean Hapke parameters for S-class asteroids given by Helfenstein and Veverka (1989): a single-scattering albedo  $w = 0.23$ , and a phase function expanded to 6th order in Legendre polynomials with a width parameter  $\xi = -0.35$ . The correction for macroscopic surface roughness from Hapke (1984) is applied with a mean slope parameter  $\bar{\theta} = 20^\circ$ ; this has no bearing on the absorbed flux but is relevant to the computation of light curves (section 3). These reflectance parameters are assumed to be constant over the surface. The opposition effect (Hapke, 2002) is ignored, as is the illumination of other parts of the surface by the reflected flux.

I neglect the effects of thermal conductivity, so that the reradiated flux exactly balances the absorbed flux at all times. Each tile is assumed to radiate isotropically; if there is no blockage by the local horizon, the outgoing photons uniformly fill the upward-facing hemisphere, and the recoil force on the tile is given by

$$f_{\text{rec}} = 2\pi \int_0^{\pi/2} \frac{F_{\text{abs}}A}{\pi c} \cos^2 \theta \sin \theta d\theta = \frac{2F_{\text{abs}}A}{3c}, \quad (2)$$

where  $A$  is the tile area,  $c$  is the speed of light, and  $\theta$  is the polar angle from the surface normal. In this case the recoil force is directed inward, normal to the surface. If, instead, part of the sky is blocked by the local horizon, some reradiated photons from the tile will strike other parts of the object, and the tile will intercept some photons reradiated by these other parts. Photons traded between different parts of the surface cannot exert a torque on the body until they are radiated into the clear sky. As a result, both the magnitude and direction of the recoil force will be changed. I compute an approximate correction for this effect, assuming that traded photons have no net effect on the energy absorbed by each tile. For the moment, suppose that the tile’s local horizon were uniformly elevated an angle  $\psi_h$

---

<sup>2</sup>“Thermophysical Asteroid Code, Obviously”

above the horizontal. Then for the same radiated flux, the intensity would be increased by a factor  $\sec^2 \psi_h$ , and the magnitude of the recoil force would be given by

$$f_{\text{rec}} = 2\pi \int_0^{\pi/2 - \psi_h} \frac{F_{\text{abs}} A}{\pi c \cos^2 \psi_h} \cos^2 \theta \sin \theta d\theta = \frac{2F_{\text{abs}} A}{3c} \left( 1 + \frac{\sin^2 \psi_h}{1 + \sin \psi_h} \right). \quad (3)$$

The force would be increased, relative to the flat-horizon case, by a factor  $1 + \sin^2 \psi_h / (1 + \sin \psi_h)$  because the elevated horizon causes the outgoing radiation to be “beamed” into a narrower solid angle. In practice, of course, the elevation of the horizon is not uniform in azimuth. Therefore I replace  $\psi_h$  with the mean elevation, given by

$$\bar{\psi}_h = \frac{1}{N_h} \sum_{i=0}^{N_h-1} \psi_h(\eta_i), \quad (4)$$

where  $\eta_i$  is the azimuth of the  $i$ th point (out of  $N_h = 50$ ) in the horizon map. The magnitude of the recoil force is then taken to be amplified by a factor  $1 + \sin^2 \bar{\psi}_h / (1 + \sin \bar{\psi}_h)$  over the flat-horizon case. The direction of  $\vec{f}_{\text{rec}}$  is taken to be antiparallel to the clear-sky normal  $\hat{N}_{\text{sky}}$ , which is computed from a first-order Fourier expansion of the horizon map:

$$\hat{N}_{\text{sky}} \equiv \frac{\vec{n}_{\text{sky}}}{n_{\text{sky}}}, \quad (5)$$

where

$$\vec{n}_{\text{sky}} = \hat{N}_{\text{surf}} - \hat{e}_n \tan \left( \frac{2}{N_h} \sum_{i=0}^{N_h-1} \psi_h(\eta_i) \cos \eta_i \right) - \hat{e}_w \tan \left( \frac{2}{N_h} \sum_{i=0}^{N_h-1} \psi_h(\eta_i) \sin \eta_i \right), \quad (6)$$

$\hat{N}_{\text{surf}}$  is the surface normal, and  $\hat{e}_n$  and  $\hat{e}_w$  are the unit vectors in the local north and west directions, respectively.

The total instantaneous torque is then simply the cross product  $\vec{r} \times \vec{f}_{\text{rec}}$ , where  $\vec{r}$  is the vector from the center of mass to the tile centroid, summed over tiles. The torque is averaged over the spin and orbital phase, assuming the periods are incommensurable. For computational simplicity, the orbit is taken to be circular. For orbits with finite eccentricity  $e$ , the averaged torque can be simply scaled by a factor  $(1 - e^2)^{-1/2}$  (Scheeres, 2007b).

## 2.2. Base Objects

I define a set of base objects, on which to measure the effects of smaller scale topography, using the “Gaussian random sphere” formalism of Muinonen and Lagerros (1998). In this approach the distance to the surface from the origin is given by

$$r(\theta, \phi) = \exp \left[ s(\theta, \phi) - \frac{\beta^2}{2} \right], \quad (7)$$

where  $(\theta, \phi)$  are the usual spherical-coordinate angles and the function  $s(\theta, \phi)$  is defined by an expansion in spherical harmonics:

$$s(\theta, \phi) = \sum_{l=0}^{\infty} \sum_{m=-l}^l s_{lm} Y_{lm}(\theta, \phi). \quad (8)$$

In this formulation, the mean radius of the body  $\bar{r} \equiv 1$ . Since  $s(\theta, \phi)$  is real, the coefficients  $s_{lm}$  are constrained by the relation

$$s_{l,-m} = (-1)^m s_{lm}^*. \quad (9)$$

For nonnegative  $m$ , each  $s_{lm}$  is a Gaussian random variable having zero expectation value and a variance given by

$$\begin{aligned} \text{Var}[\Re(s_{lm})] &= (1 + \delta_{m0}) \frac{2\pi}{2l+1} C_l; \\ \text{Var}[\Im(s_{lm})] &= (1 - \delta_{m0}) \frac{2\pi}{2l+1} C_l. \end{aligned} \quad (10)$$

In eq. (10),  $\delta_{ij}$  is the Kronecker delta symbol;  $C_l$  represents the coefficients of the Legendre expansion of the log-radius covariance function, which also define the quantity  $\beta \equiv (\sum_l C_l)^{1/2}$  in eq. (7). Muinonen and Lagerros (1998)

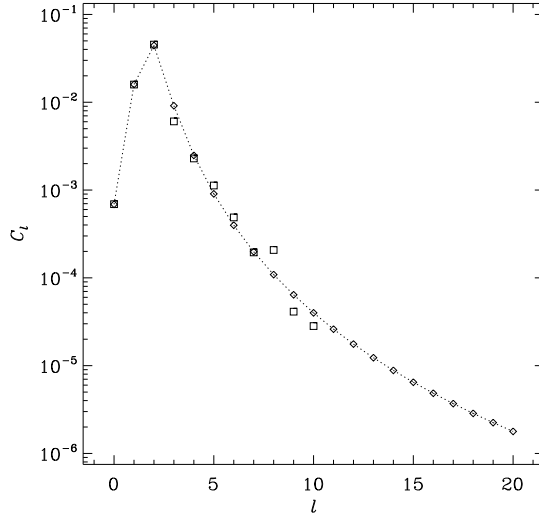


Figure 1: Coefficients of the Legendre expansion of the log-radius covariance function. *Squares*: as tabulated by Muinonen and Lagerros (1998). *Diamonds and dotted line*: from the adopted fit, Eq. (11).

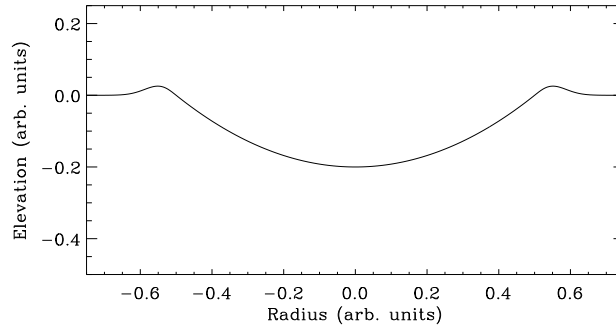


Figure 2: Crater profile according to Eq. (12), with depth to diameter ratio  $q = 0.2$  and rim width  $\delta = D/20$ .

estimate the  $C_l$  coefficients for  $l \leq 10$  from shapes fitted to light curve observations of 14 objects. For this work I adopt an analytic fit to the results for their small-object subsample (4th column of their Table 3), given by

$$C_l = 1.2 \frac{(l^2 + 0.26)^2}{(l^8 + 90.0)^{1.06}}. \quad (11)$$

Fig. 1 shows the coefficients from Muinonen and Lagerros (1998) and the fit. This fit will be used below to extrapolate the covariance function out as far as  $l = 40$ . For  $l \gg 1$ , Eqs. (10) and (11) imply  $C_l \sim l^{-4.48}$ , so that the RMS amplitudes  $s_{lm}$  decline as  $l^{-2.74}$ .

Each base object is a Gaussian random sphere with the expansion in Eq. (8) truncated at a maximum order  $l_{\text{base}}$ . I adopt values of  $l_{\text{base}} = 4, 5, 7, 9, 12, 15, 20$ , and, for each value, compute 6 different base objects with independent random realizations of the  $s_{lm}$  coefficients.

### 2.3. Addition of Small-Scale Topography

The base objects are intended to represent asteroids whose shapes are constrained by observations down to some minimum angular scale. Different types of small-scale topographic structure can be added to the base objects. In

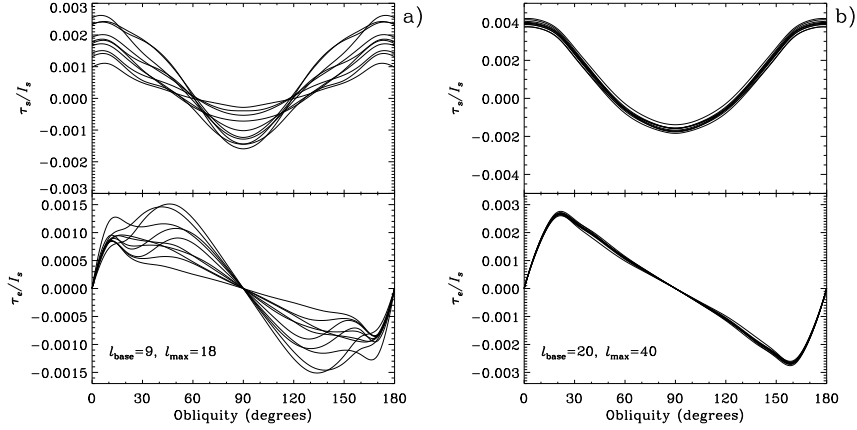


Figure 3: Typical variation in YORP torques caused by Gaussian topographic power added at smaller scales to the base objects. (a) Base object with  $l_{\text{base}} = 9$ , topography added to  $l_{\text{max}} = 18$ . Top- and bottom-most curves correspond to the objects shown in Fig. 4. (b) Base object with  $l_{\text{base}} = 20$ , topography added to  $l_{\text{max}} = 40$ . Top panels show the spin component, and bottom panels the obliquity component, of the torque, normalized by the moment of inertia about the short (spin) axis, plotted against obliquity. Individual curves correspond to ten different random realizations of the added topography.

Section 3 I measure the separate effects on YORP of each of the following:

1. *Gaussian power at smaller scales.* Here the expansion in Eq. (8) is simply extended from  $l_{\text{base}}$  to some higher maximum order  $l_{\text{max}}$ . The  $s_{lm}$  coefficients are identical to those for the base object for  $l \leq l_{\text{base}}$ , and chosen randomly according to Eq. (10) for  $l_{\text{base}} < l \leq l_{\text{max}}$ .
2. *Craters.* One or more circular craters are placed randomly on the surface. The crater depth  $z$  as a function of radius  $r$  from its center is given by

$$z(r) = qD \left( 1 - 4 \frac{r^2}{D^2} \right) \times \begin{cases} 1, & \text{if } r \leq D/2; \\ \exp \left[ -\frac{(r-D/2)^2}{2\delta^2} \right], & \text{if } D/2 < r \leq D/2 + 3\delta. \end{cases} \quad (12)$$

In Eq. (12),  $D$  is the crater diameter,  $q$  is the depth-to-diameter ratio, and  $\delta$  is the width of the raised rim. I adopt  $q = 0.2$  and  $\delta = D/20$ , based on NEAR-Shoemaker observations of 253 Mathilde (Thomas et al., 1999) and 433 Eros (Veverka et al., 2001; Thomas et al., 2002) and laboratory impact experiments (Nakamura, 2002; Housen and Holsapple, 2003). The resulting profile is shown in Fig. 2. The vertical displacement  $z$  is in the direction of the mean surface normal of the area the crater will occupy. Preexisting topography is first flattened to the level of the mean surface and then overwritten by the crater. Multiple craters are added sequentially so that overlapping features are reasonably realistic.

3. *Boulders.* One or more boulders can also be placed on the surface. As a crude representation of a boulder, the tile vertices falling within a given radius of the boulder center are raised, creating an approximately round, mesa-like feature with jagged edges. As with craters, the existing topography is first flattened so that the boulder's upper surface is featureless.

For each object, the center of mass and inertia tensor are calculated after the small-scale topography is added, assuming a homogeneous density  $\rho$ . The coordinate system is shifted and rotated to align the origin with the center of mass and the coordinate axes with the principal axes of the body. All objects are assumed to be rotating about the shortest principal axis.

### 3. Results

#### 3.1. Gaussian Power at Smaller Scales

Any set of observations will be able to constrain the topographic power down to some minimum length scale or maximum harmonic order. As a straightforward indicator of the effect of neglected higher orders, I add power to each

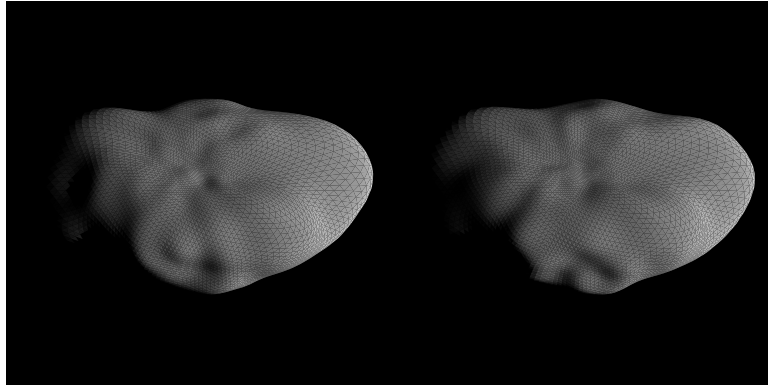


Figure 4: Identical views of the two  $l_{\text{base}} = 9$  objects from Fig. 3a with the (*left*) smallest and (*right*) largest torques. Line of sight is in the plane containing the short and middle axes of the body,  $45^\circ$  from each, and the illumination is from the right at  $45^\circ$  phase angle.

base object to a maximum order  $l_{\text{max}} = 2l_{\text{base}}$ , and measure the error in torque incurred by ignoring topography down to half the observationally constrained scale.

Fig. 3 shows typical results for two of the 42 base objects, one with  $l_{\text{base}} = 9$  and one with  $l_{\text{base}} = 20$ , corresponding to minimum angular scales of  $40^\circ$  and  $18^\circ$ , respectively. The curves show the averaged torque components affecting the spin rate ( $\tau_s$ ) and the obliquity ( $\tau_e$ ), normalized by the principal moment of inertia about the short axis  $I_s$ , plotted against obliquity.<sup>3</sup> Different curves indicate the 10 random realizations of the added topography. Clearly, knowing the topography only to order  $l_{\text{base}} = 9$  (Fig. 3a) is not sufficient to determine the torque to even order-unity accuracy. The range in  $\tau_s$  spans nearly a factor of 3 at obliquity  $\epsilon = 0^\circ$ , and more than a factor of 5 at  $\epsilon = 90^\circ$ . The location of the ‘‘Slivan states’’ (Slivan, 2002), which require  $\tau_s = 0$ , varies over  $15^\circ$ ; and the obliquity torque  $\tau_e$  in the vicinity of the Slivan states varies over a factor of 5. In contrast, the  $l_{\text{base}} = 20$  objects (Fig. 3b), to which power has been added to  $l_{\text{max}} = 40$ , have largely concordant torques. Evidently, at sufficiently small angular scales, the neglect of Gaussian power at still smaller scales is not too serious, as long as it follows a simple extrapolation of the covariance coefficients.

As a measure of how wrong a YORP prediction is likely to be due to neglect of the smaller scale topography, I compute, at each value of obliquity, the standard deviation in each torque component over the 10 trials, then average over obliquity; this quantity is normalized to the mean absolute value of that component, also averaged over obliquity. The result is an obliquity-independent measure of the expected relative error. For the  $l_{\text{base}} = 9$  case in Fig. 3a, the expected relative errors are 38% in  $\tau_s$  and 32% in  $\tau_e$ . Keep in mind that these are  $1\sigma$  errors, implying 95% confidence bands (for a Gaussian distribution) with full widths of 152% and 128%, consistent with the order-unity variation seen in the figure. For the  $l_{\text{base}} = 20$  case, the relative  $1\sigma$  errors are 7% and 3% in  $\tau_s$  and  $\tau_e$  respectively. I will use this same approach to quantify the effects of craters and boulders below.

The most remarkable thing about the results in Fig. 3a is that the individual objects, despite differing by factors of a few in their YORP torques, appear nearly identical. Fig. 4 shows a representative view of the two objects in Fig. 3a having the most discordant torques. To assess whether these objects would be distinguishable photometrically, I compute optical light curves over a grid of 40 rotation pole directions and 10 phase angles from  $0^\circ$  to  $90^\circ$ . I find that the RMS photometric difference between these two objects is  $< 0.05$  magnitudes at all phase angles. The *maximum* difference is  $< 0.1$  mag at phase angles  $\leq 50^\circ$ , and is  $> 0.2$  mag only at phase angles of  $75^\circ$  or higher, making it unlikely that these objects would be distinguished by groundbased observations.

In Fig. 5, I show the relative 1-sigma errors for all of the base objects. The scatter at each  $l_{\text{base}}$  reflects the base objects’ different YORP susceptibilities. One can easily see that order-unity errors in the torque should be expected for  $l_{\text{base}} \leq 10$ . To be reasonably confident of errors under 10%, the surface must be known to at least  $l_{\text{base}} = 20$ . Owing to

<sup>3</sup>Numerical results for normalized torques are given in units of  $1.52 \times 10^{-15} (\rho/2 \text{ g cm}^{-3})^{-1} (\bar{r}/1 \text{ km})^{-2} (a/1 \text{ AU})^{-2} (1 - e^2)^{-1/2} \text{ s}^{-2}$ , where  $\rho$  and  $\bar{r}$  are the constant density and mean radius of the body, and  $a$  and  $e$  are the orbital semimajor axis and eccentricity.

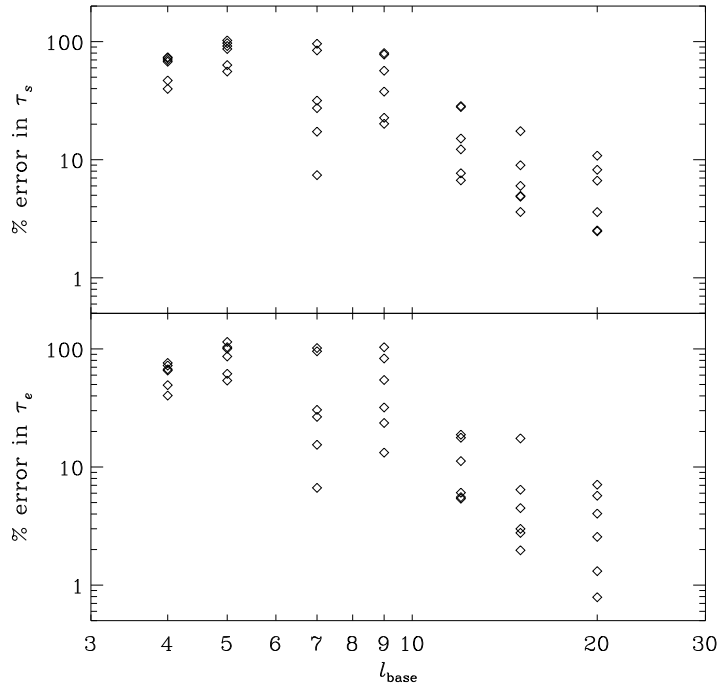


Figure 5: Expected relative  $1\sigma$  error in the YORP torque caused by neglecting Gaussian topographic power at  $l_{\text{base}} < l \leq 2l_{\text{base}}$ . *Top*: error in the spin component; *bottom*: error in the obliquity component. The relative error is the standard deviation in each component over 10 random trials, averaged over obliquity, and normalized to the mean absolute value of that component. Multiple symbols correspond to 6 different base objects at each  $l_{\text{base}}$ .

the steepness of the extrapolated covariance function, most of the change in the torque is actually produced by orders close to  $l_{\text{base}}$ . Fig. 6 shows the relative errors for the  $l_{\text{base}} = 12$  objects with power added to  $l_{\text{max}} = 13, 14, 16, 18, 24,$  and  $36$ . There is no discernible increase in the error for  $l_{\text{max}} > 18$ , and the single order  $l = 13$  seems to be responsible for roughly half of the asymptotic value.

### 3.2. Craters

Actual small-scale topography is likely to be non-Gaussian. Impact craters are one example of Poisson-distributed features not well described by a truncated spherical-harmonic expansion. The crater size distribution has been estimated for 951 Gaspra (Chapman et al., 1996b; Greenberg et al., 1994), 243 Ida (Belton et al., 1994; Chapman et al., 1996a), 253 Mathilde (Chapman et al., 1999), and 433 Eros (Chapman et al., 2002). To lowest order, the cumulative distribution of craters with diameters larger than  $D$ ,  $N(D)$ , is reasonably well approximated by a power law,  $N(D) \sim D^{-2}$  (O’Brien et al., 2006). Though there are significant deviations in the logarithmic slope for different objects, the known distributions all describe a steeply diminishing number of large craters. The largest craters have diameters ranging from 0.35 to 1.2 times the bodies’ mean radii (Thomas et al., 1999).

I return to the original base objects, removing the small-scale Gaussian power added in Section 3.1, in order to measure separately the effect of craters on the YORP torque components. I start by randomly placing a single, modest-sized crater of diameter  $D = 0.3$  (in units of the body mean radius) on the base objects. Fig. 7 shows the resulting relative  $1\sigma$  errors, calculated as in Sec. 3.1 with ten random crater placements for each object. A single crater can clearly alter the spin and obliquity torques by tens of percent, even though the crater itself, including the raised rim, occupies only  $\sim 0.5\%$  of the total surface. The effect increases with  $l_{\text{base}}$  at values  $l_{\text{base}} \lesssim 9$ . A similar, but less pronounced, increase is also seen in the Gaussian case (Fig. 5). The single crater actually produces less error



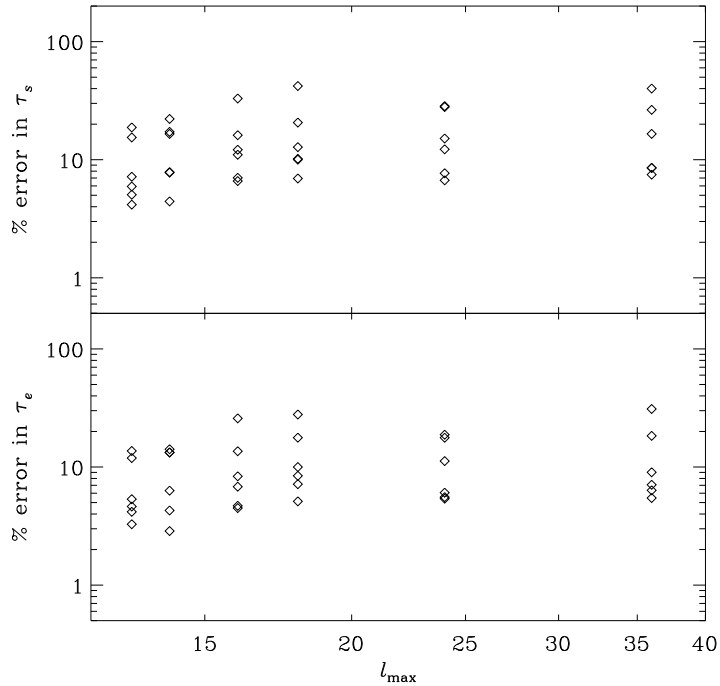


Figure 6: Expected relative  $1\sigma$  error, as in Fig. 5, for the  $l_{\text{base}} = 12$  base objects with Gaussian power added to  $l_{\text{max}} = 13, 14, 16, 18, 24, 36$ . There is no strong dependence on  $l_{\text{max}}$  for  $l_{\text{max}} > 18$ , indicating that orders just above the cutoff  $l_{\text{base}}$  are most important.

for  $l_{\text{base}} \lesssim 9$  than does small-scale Gaussian power added to the same base object. But the effect of the crater for  $l_{\text{base}} > 10$  is larger than the Gaussian case and, to within the statistical errors, independent of the base order. This may be due either to the declining amplitudes  $C_l$  at higher  $l$  or to the fact that  $l = 9$  corresponds roughly to the scale of the crater itself. Evidently the crater couples to other mesoscale surface features of roughly its own size more effectively than to the large-scale structure at smaller  $l$ .

Fig. 8a shows the normalized torque as a function of obliquity for ten random placements of single craters on the same  $l_{\text{base}} = 20$  base object used in Fig. 3b. The effect of the crater is about twice that of the added Gaussian topography: the relative errors in  $\tau_s$  and  $\tau_e$  are 14% and 6%, respectively, which also represent median results over all base objects. Fig. 8b shows the effect of doubling the crater size to  $D = 0.6$  on the same base object. The relative errors increase to 56% and 14%. Comparing the extreme examples (the highest and lowest curves), the spin components differ by a factor of 4.4 at  $\epsilon = 90^\circ$  and actually have opposite signs at  $\epsilon = 0^\circ$ . Fig. 9 shows these two most discordant objects, which turn out to be cratered at almost diametrically opposite positions.

Cratering a base object moves the center of mass and slightly reorients the principal axes. To determine whether these adjustments contribute to the change in torque, I recompute the torques for 60 of the cratered and bouldered (see Section 3.3) objects, without shifting to the new center of mass or reorienting to the new principal axes. For either craters or boulders, the results differ, on average, by only a few percent, indicating that it is really the surface topography that is responsible for the large expected torque errors.

The objects, even those with single large ( $D = 0.6$ ) craters, are so photometrically similar that it is unlikely that they would be distinguishable in current light curve programs. To assess this possibility, I take all 60 of the  $l_{\text{base}} = 20$  cratered objects and compute light curves over the same grid of 40 orientations and 10 phase angles used in section 3.1. I then calculate the probability that two objects, differing only in crater location, would be observed at a given moment to have a magnitude difference  $> \Delta$ . The result, as a function of phase angle, is shown in Fig. 10. Note

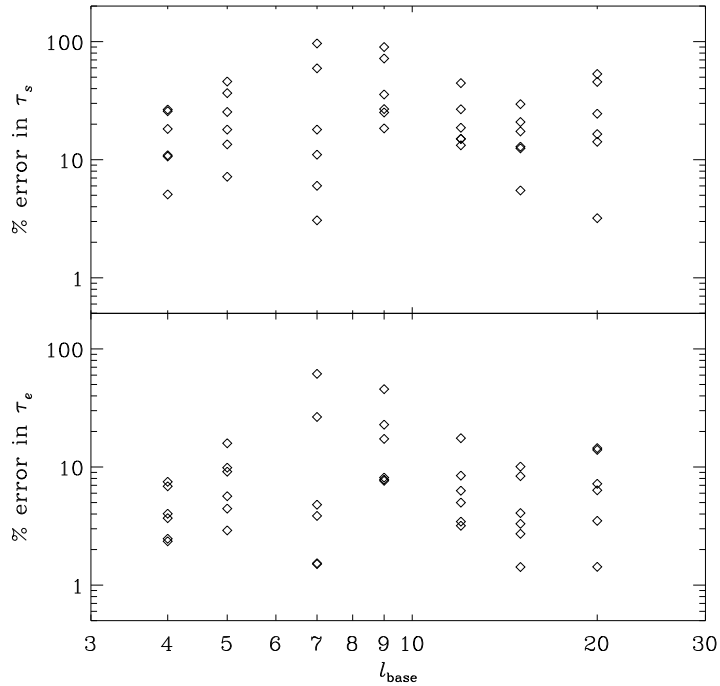


Figure 7: Expected relative  $1\sigma$  standard deviation in the YORP torque, as in Fig. 5, caused by a single randomly placed crater with diameter  $D = 0.3$  added to different base objects.

that, unless substantial data are obtained at phase angles  $> 70^\circ$ , one expects that no more than 1% of the total data will differ by more than 0.05 mag, and no more than 0.01% by more than 0.1 mag. In practice, observations at phase angles above  $45^\circ$  are rare in light curve programs.

Fig. 11 shows the scaling of the relative torque errors with crater size. The diamonds and plus signs show results for single-cratered objects with  $l_{\text{base}} = 12$  and 20, respectively. One might naively expect the torque error to scale with the crater area ( $\sim D^2$ ); and Fig. 11 shows that this is not a bad description for  $D > 0.3$ . However, at smaller diameters the scaling is much steeper, with the relative error roughly  $\propto D^3$ . This nonlinear response may be attributable to shadowing, although the same steepening does not occur for boulders (Section 3.3 below). The squares and crosses in Fig. 11 (slightly offset for clarity) indicate the results for objects with four  $D = 0.3$  craters each. Since the changes in torque produced by each added crater are random and uncorrelated, one should expect the total change to scale as the square root of the number of craters. This expectation is confirmed by the factor 2 increase in the relative errors over the single-crater case. The implications of these scaling laws for the expected accuracy of YORP predictions on realistically cratered objects are discussed in section 4 below.

### 3.3. Boulders

Boulders are a second example of Poisson-distributed topography. The surface of 25143 Itokawa has been found to be dominated by boulders, with a cumulative size distribution well represented by  $N(D) \propto D^{-3}$  over a factor 10 in diameter; the largest boulder, Yoshinodai, is fully one-tenth the size of its parent body (Saito et al., 2006). For 433 Eros, Chapman et al. (2002) obtain a result consistent with  $N(D) \propto D^{-4}$ . These size distributions are substantially steeper than those for craters; thus one can expect the cumulative effect of moderate sized boulders to be more relatively important than that of moderate sized craters.

I proceed with the same strategy to assess the influence of boulders on YORP torques. I add a single mesa-shaped boulder, with diameter  $D = 0.3$  (in units of the body mean radius) and height  $h = D/2$ , at random locations to the base

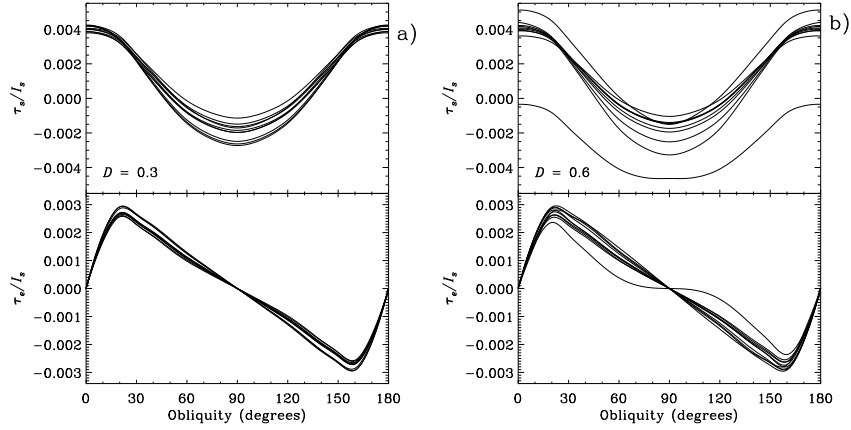


Figure 8: Typical variation in YORP torques caused by single craters of diameter (a)  $D = 0.3$ , (b)  $D = 0.6$ , randomly placed on the same base object used in Fig. 3b. Top- and bottom-most curves correspond to the objects shown in Fig. 9.

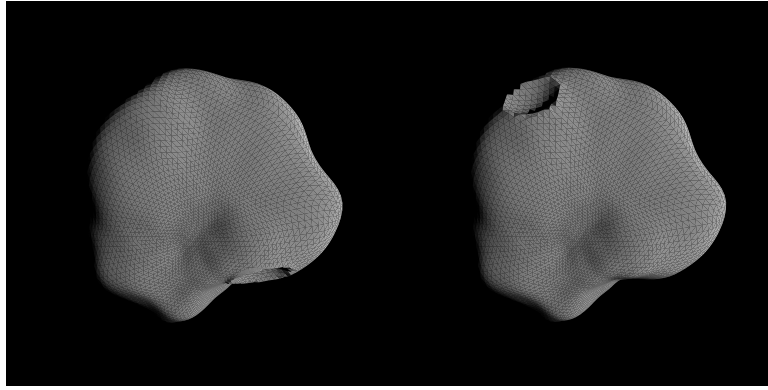


Figure 9: Identical views, along the rotation axis, of the two objects having the (left) smallest and (right) largest torques in Fig. 8b.

objects. The base objects have mean longest diameters of approximately 3.1, so the size of these boulders relative to their parent bodies approximately matches that of Yoshinodai. The height-to-diameter ratio corresponds to typical values measured for boulders on 433 Eros (Thomas et al., 2002).

Fig. 12 shows the expected relative error in the torque components caused by the single large boulder. The effect is quite dramatic: typical  $1\sigma$  errors are 10% to 100% in the spin component, and 5% to 50% in the obliquity component. This is roughly a factor 3 larger than the effect of craters of the same diameter, though the difference may be attributable to the simple fact that boulders can be proportionally taller than craters are deep (here, by a factor of 2.5). As in the case of craters, there is a weak increase in the mean error for values of  $l_{\text{base}} < 10$ , but little difference is seen at higher order. The scaling of the errors with boulder size is shown in Fig. 13. The boulders are all similarly shaped, with  $h = D/2$ . The relative error scales quite cleanly as  $D^2$ , i.e., proportional to the boulder surface area.

Examples of the torque components as a function of obliquity are shown in Fig. 14a, for 10 random  $D = 0.3$  boulder placements on the same  $l_{\text{base}} = 20$  object used in Figs. 3b and 8. This case again represents a typical amount of topographically induced variation. Boulders have a tendency to shift the curves for  $\tau_s/I_s$  up and down while altering the overall amplitude of those for  $\tau_e/I_s$ . Note that the sign of the spin torque can be flipped by the location of a single boulder, even for this unexceptional object. A more extreme example is seen in Fig. 14b, which shows the same curves for one of the other five  $l_{\text{base}} = 20$  objects. Here the sign of the spin torque at all obliquities can be reversed by the location of a single Yoshinodai-sized boulder. The two most discordant objects are shown in Fig. 15. The boulder

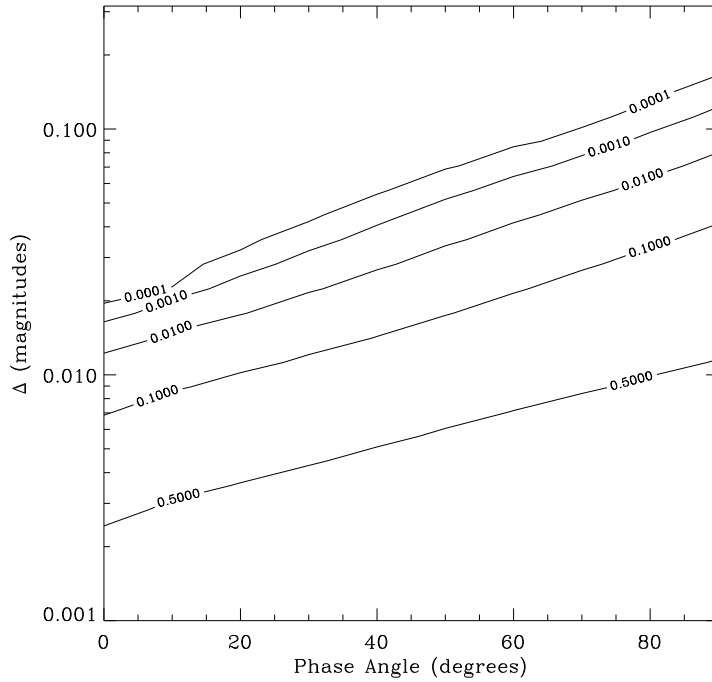


Figure 10: Probability contours for observing a photometric difference  $\Delta$  or larger, as a function of phase, between pairs of objects that differ only in the location of a single crater of diameter  $D = 0.6$ . Results shown are averaged over the 6 base objects with  $l_{\text{base}} = 20$ .

location differs by barely twice its own diameter; yet the object on the left will inexorably spin up while the object on the right will spin down.

#### 4. Discussion

The above results indicate that sensitivity to small-scale topography is an inherent characteristic of the YORP effect. Since YORP operates by virtue of the non-cancellation of many independent torque components that vary across the surface, over the rotation of the body, and around the orbit, this conclusion is perhaps not surprising; however, it does impose strong limits on the predictability of YORP torques, and has important consequences for the spin evolution of small bodies.

If the surface is describable by a spherical harmonic expansion whose coefficients are Gaussian-distributed, the topography must be known accurately at least to harmonic order  $l = 10$  to allow a YORP prediction of even the correct sign. To achieve 10% accuracy requires the surface to be known at least to  $l = 20$ , if the topography diminishes with  $l$  in a manner consistent with a simple extrapolation of the Muinonen and Lagerros (1998) covariance coefficients (Eq. [11]). Few objects can be modeled reliably at this resolution. Furthermore, actual small scale topography is not Gaussian and not small in amplitude. The above results show that Poisson-distributed features such as craters and boulders, which produce substantial shadowing and which are not well revealed by groundbased observations, can have significant effects. A single large feature can alter YORP torques by tens of percent or more.

I found above that the relative torque error scales as  $\sigma \sim D^\beta$ , where  $\beta \approx 2$  for boulders and  $2 \lesssim \beta \lesssim 3$  for craters. Using these numerical results and the observed size distributions, one can estimate the relative influence of large and small craters and boulders. The observed cumulative counts are reasonably well represented by  $N(D) \sim D^{-\alpha}$ , with

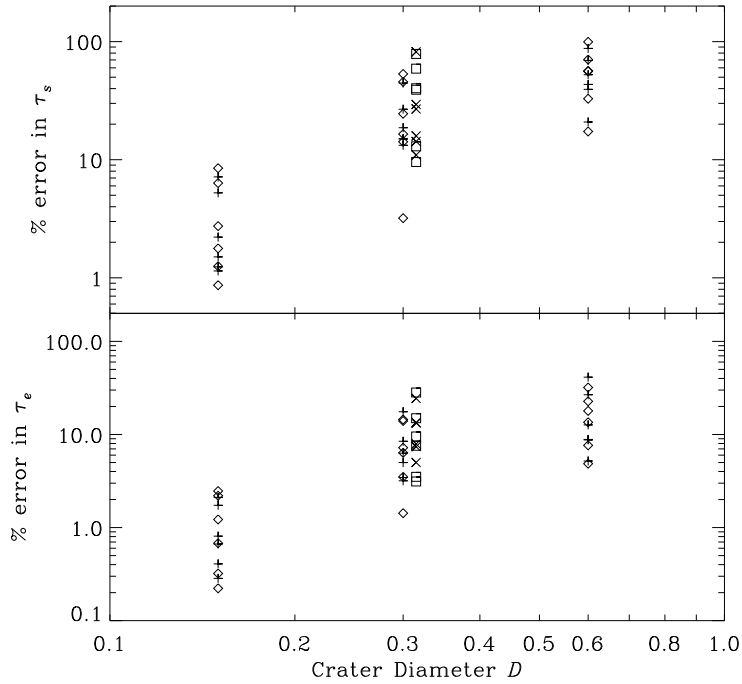


Figure 11: Expected relative error in torque, as in Fig. 7, caused by single craters randomly placed on base objects with  $l_{\text{base}} = 12$  (*plus signs*) and  $l_{\text{base}} = 20$  (*diamonds*), as a function of crater diameter  $D$ . *Crosses* and *squares* (offset horizontally) show results for 4 randomly placed craters each of diameter  $D = 0.3$ , on objects with  $l_{\text{base}} = 12, 20$  respectively.

$3 \lesssim \alpha \lesssim 4$  for boulders and  $1 \lesssim \alpha \lesssim 2$  for craters.<sup>4</sup> Assuming the effects of individual boulders or craters to be uncorrelated, one expects in either case that the variance in torque produced by features with diameters between  $D_{\text{min}}$  and  $D_{\text{max}}$  will scale according to

$$\sigma^2 \propto \int_{D_{\text{min}}}^{D_{\text{max}}} \frac{dN}{dD} D^{2\beta} dD \propto D_{\text{max}}^{2\beta-\alpha} - D_{\text{min}}^{2\beta-\alpha}, \quad (\alpha \neq 2\beta). \quad (13)$$

For cratered objects, Eq. (13) implies that at least 75% of the total variance (87% of the expected  $\sigma$ ) is produced by the 4 biggest craters. Fig. 11 shows that the expected error from the random location of the single largest crater is already approaching 100% at  $D_{\text{max}} = 0.6$ , close to the observed maximum diameter on Eros but rather modest compared to the values of 0.89 and 1.2 for Ida and Mathilde, respectively (Thomas et al., 1999). These very large craters could possibly give rise to noticeable features in high phase-angle light curves; however, light curve inversion performs poorly in recovering surface concavities because the inversion problem is non-unique (Kaasalainen et al., 1992; Kaasalainen and Torppa, 2001). The convex, pre-encounter model of the *Rosetta* target 2867 Steins (Lamy et al., 2008) resembles the *in situ* images,<sup>5</sup> but by construction misses several large craters, including one with an apparent diameter  $D \approx 0.9$ . A non-convex inversion probably would not have revealed this crater, as the light curve data are limited to phase angles  $< 42^\circ$ . Convex models, in general, may be useful for determining overall surface reflectance and thermal properties, and may give accurate predictions for Yarkovsky accelerations. But a YORP prediction based on a convex model is likely to be wrong by of order 100%.

<sup>4</sup>As before, diameters are implicitly in units of the body mean radius.

<sup>5</sup>[http://www.esa.int/SPECIALS/Rosetta/SEMNM04KKF\\_0.html](http://www.esa.int/SPECIALS/Rosetta/SEMNM04KKF_0.html)

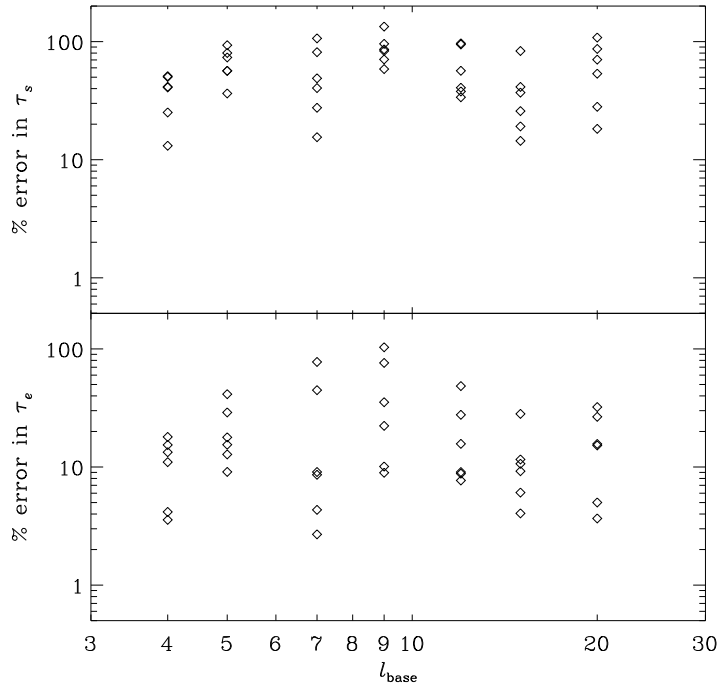


Figure 12: Expected relative  $1\sigma$  standard deviation in the YORP torque, as in Fig. 5, caused by a single randomly placed boulder with diameter  $D = 0.3$  added to different base objects.

Boulders, because of their steeper size distribution, behave differently: *at most* half of the total variance is produced by boulders larger than half the maximum size. In fact, if the distribution is as steep as on Eros ( $\alpha = 4$ ), then the variance is formally divergent as  $D \rightarrow 0$ . Of course, distributions  $dN/dD \sim D^{-1}$  or steeper are unphysical in this limit; but the scaling indicates that the YORP torque can be affected as much by the surface distribution of small boulders as by that of large ones. The results of section 3 also show that single boulders may have significantly greater effect on the torque than craters of the same size; a single Yoshinodai-sized object can easily alter the spin torque by tens of percent, and in some cases change its sign. The clear implication is that the surface boulder distribution can be critical in determining the actual consequences of YORP.

Thus, one should expect uncertainties of order unity in predictions of the YORP effect made from models derived from remote observations, just from the unconstrained nature of the small-scale surface topography. The true situation is actually even worse, since I have neglected other issues, such as variations in albedo, surface roughness, and internal density, which probably have comparable effects. Indeed, Scheeres and Gaskell (2008) find that shifting the center of mass of Itokawa by only 15 m can reverse the sign of the spin torque. At present, there have been 4 attempts to predict the YORP acceleration from groundbased data and compare with direct measurements. In one case (1682 Apollo), the correct magnitude and sign were obtained, with an uncertainty of  $\pm 25\%$ ; in a second (54509 YORP), models gave the correct sign but the wrong magnitude by a factor of 2 to 7. In the third (25143 Itokawa), pre-Hayabusa models evidently obtained the wrong sign (compared to later models), but the predicted acceleration has still not been detected. And in the fourth (1620 Geographos), torques computed for different convex shape models bracketed the observed value, but varied over a factor of 5. This situation is about what we should expect. Generally speaking, a YORP prediction computed from a groundbased model will be accurate only to within factors of order unity, and will have no better than an 80% chance of having the correct sign.

The sensitivity of reradiation torques to boulders also implies that there may be substantial stochasticity in the spin

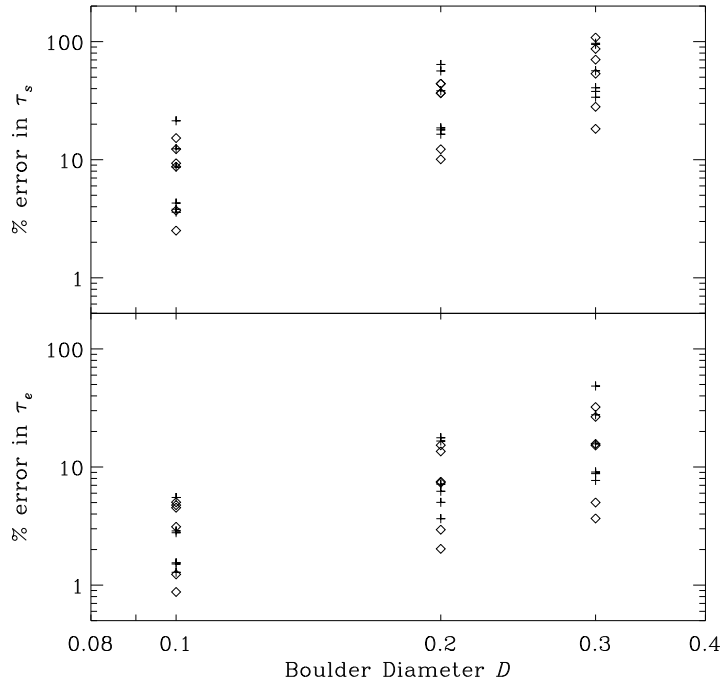


Figure 13: Expected relative error in torque, as in Fig. 12, caused by single boulders, as a function of boulder diameter  $D$ . Symbols have the same meaning as in Fig. 11.

evolution of small bodies under the influence of YORP. In the standard picture of the YORP cycle (Rubincam, 2000), an object can gradually spin up, simultaneously evolving in obliquity, as determined by the now familiar “YORP curves” (e.g., Figs. 3, 8, and 14). In most cases, spin-up continues only until reaching an orientation regime where  $\tau_s < 0$ . The object then spins down, asymptotically approaching the stable fixed point in obliquity. Objects with substantial power in the higher YORP orders (Nesvorný and Vokrouhlický, 2007, 2008) can sometimes have stable fixed points at obliquities where  $\tau_s > 0$ ; examples of this behavior are seen in Figs. 8b and 14b, along with cases where  $\tau_s > 0$  at all obliquities. These objects would presumably spin up indefinitely. But a new possibility raised here is that a seemingly minor topographic change, such as the movement of a boulder, can stochastically shift the evolution onto a new set of YORP curves. One would expect such events to occur well before catastrophic fissioning or even unbinding of surface material, as the local effective gravity vectors change with the accelerating spin. Calculations for contact-binary configurations (Scheeres, 2007a) and numerical experiments on rubble piles (Walsh et al., 2008; Harris et al., 2009) confirm that surface changes occur at rotation rates slower, by factors of several, than the nominal centrifugal limit for self-gravitating spheres. The latter corresponds to the observed minimum rotation periods of large asteroids, at approximately 2 hours. Thus a broad range of spin periods, from 2 to perhaps 10 hours, may correspond to a “scattering zone”, in which small topographical changes stochastically reverse the YORP torques. An object being spun up by YORP may scatter multiple times through motion or loss of surface boulders, random-walking up and down in spin rate, before finally crossing the actual spin limit and either fissioning or shedding all loose objects. It is extremely interesting that the observed distribution of NEOs in the diameter-rotation period plane (e.g., Fig. 1 of Holsapple, 2007, Statler et al. 2009, in preparation) shows the sharp cutoff at 2 hours becoming notably indistinct at diameters  $\lesssim 1$  km, where YORP is expected to become dominant. Similarly, small, fast-rotating objects approaching the higher spin limit imposed by tensile strength (Holsapple, 2007) may wander up and down in spin rate, driven not by catastrophic fragmentation, but merely by a subtle rearrangement of the surface that reverses the YORP effect.

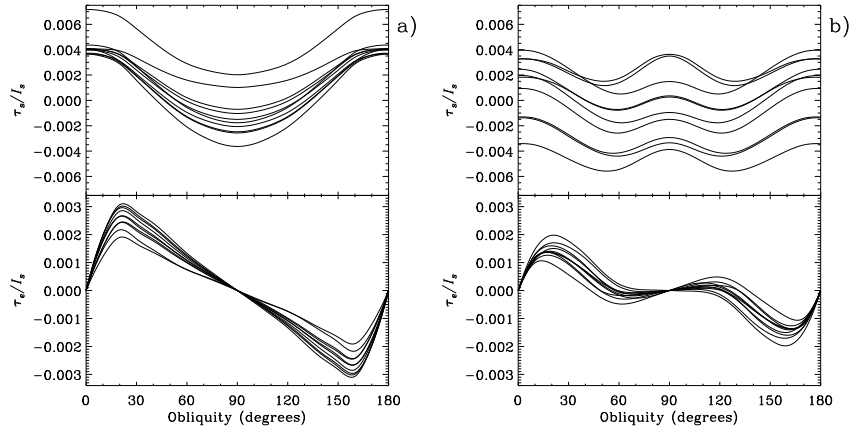


Figure 14: Typical variation in YORP torques caused by single boulders of diameter  $D = 0.3$ , randomly placed on (a) the same base object used in Figs. 3b and 8, and (b) a second object with  $l_{\text{base}} = 20$ , showing more extreme variation. Top- and bottom-most curves correspond to the objects shown in Fig. 15. Note in (b) the possibility of reversing the sign of the spin torque at all obliquities simply by repositioning one boulder.

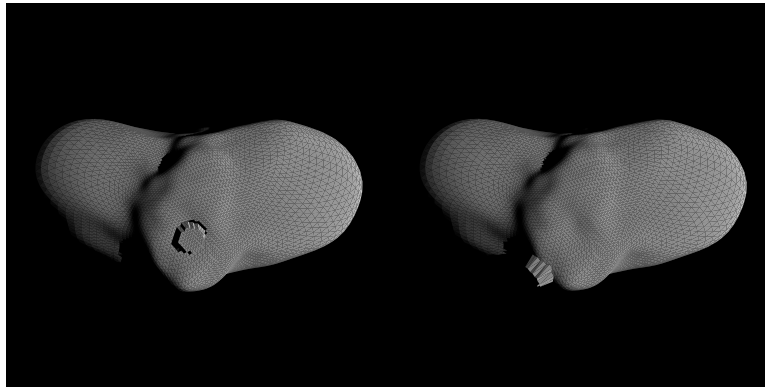


Figure 15: Identical views of the two objects from Fig. 14b with the (left) most positive and (right) most negative spin torques. Line of sight is in the plane containing the short and middle axes of the body,  $45^\circ$  from each, and the illumination is from the right at  $30^\circ$  phase angle. Moving the boulder by only twice its own diameter reverses the sign of the spin torque.

The author is grateful to David Riethmiller, Desiree Cotto-Figueroa, and Kyle Uckert for their assistance in the development of TACO; to Nalin Samarasinha, Dan Scheeres, Mangala Sharma, and Desiree Cotto-Figueroa for extensive comments on the manuscript; and to the referees, David Vokrouhlický and David Rubincam, for important suggestions that improved the paper. This work has made use of NASA's Planetary Data System and Astrophysics Data System Bibliographic Services.

## References

- Belton, M. J. S., Chapman, C. R., Veverka, J., Klaasen, K. P., Harch, A., Greeley, R., Greenberg, R., Head, III, J. W., McEwen, A., Morrison, D., Thomas, P. C., Davies, M. E., Carr, M. H., Neukum, G., Fanale, F. P., Davis, D. R., Anger, C., Gierasch, P. J., Ingersoll, A. P., Pilcher, C. B., 1994. First Images of Asteroid 243 Ida. *Science* 265, 1543–1547.
- Bottke, W. F., Morbidelli, A., Jedicke, R., Petit, J.-M., Levison, H. F., Michel, P., Metcalfe, T. S., 2002. Debaised Orbital and Absolute Magnitude Distribution of the Near-Earth Objects. *Icarus* 156, 399–433.
- Bottke, W. F., Vokrouhlický, D., Brož, M., Nesvorný, D., Morbidelli, A., 2001. Dynamical Spreading of Asteroid Families by the Yarkovsky Effect. *Science* 294, 1693–1696.
- Bottke, Jr., W. F., Vokrouhlický, D., Rubincam, D. P., Nesvorný, D., 2006. The Yarkovsky and Yorp Effects: Implications for Asteroid Dynamics. *Annual Review of Earth and Planetary Sciences* 34, 157–191.



- Breiter, S., Michalska, H., 2008. YORP torque as the function of shape harmonics. *Mon. Not. R. Astron. Soc.* 388, 927–944.
- Chapman, C. R., Merline, W. J., Thomas, P., 1999. Cratering on Mathilde. *Icarus* 140, 28–33.
- Chapman, C. R., Merline, W. J., Thomas, P. C., Joseph, J., Cheng, A. F., Izenberg, N., 2002. Impact History of Eros: Craters and Boulders. *Icarus* 155, 104–118.
- Chapman, C. R., Ryan, E. V., Merline, W. J., Neukum, G., Wagner, R., Thomas, P. C., Veverka, J., Sullivan, R. J., 1996a. Cratering on Ida. *Icarus* 120, 77–86.
- Chapman, C. R., Veverka, J., Belton, M. J. S., Neukum, G., Morrison, D., 1996b. Cratering on Gaspra. *Icarus* 120, 231–245.
- Chesley, S. R., Ostro, S. J., Vokrouhlický, D., Capek, D., Giorgini, J. D., Nolan, M. C., Margot, J.-L., Hine, A. A., Benner, L. A. M., Chamberlin, A. B., 2003. Direct detection of the yarkovsky effect by radar ranging to asteroid 6489 golevka. *Science* 302 (5651), 1739–1742.
- Đurech, J., Kaasalainen, M., Marciniak, A., Allen, W. H., Behrend, R., Bembrick, C., Bennett, T., Bernasconi, L., Berthier, J., Bolt, G., Boroumand, S., Crespo da Silva, L., Crippa, R., Crow, M., Durkee, R., Dymock, R., Fagas, M., Fauerbach, M., Fauvaud, S., Frey, M., Gonçalves, R., Hirsch, R., Jardine, D., Kamiński, K., Koff, R., Kwiatkowski, T., López, A., Manzini, F., Michałowski, T., Pacheco, R., Pan, M., Pilcher, F., Poncy, R., Pray, D., Pych, W., Roy, R., Santacana, G., Slivan, S., Sposetti, S., Stephens, R., Warner, B., Wolf, M., 2007. Physical models of ten asteroids from an observers' collaboration network. *Astron. Astrophys.* 465, 331–337.
- Đurech, J., Vokrouhlický, D., Kaasalainen, M., Higgins, D., Krugly, Y. N., Gaftonyuk, N. M., Shevchenko, V. G., Chiorny, V. G., Hamanowa, H., Hamanowa, H., Reddy, V., Dyvig, R. R., 2008a. Detection of the YORP effect in asteroid (1620) Geographos. *Astron. Astrophys.* 489, L25–L28.
- Đurech, J., Vokrouhlický, D., Kaasalainen, M., Weissman, P., Lowry, S. C., Beshore, E., Higgins, D., Krugly, Y. N., Shevchenko, V. G., Gaftonyuk, N. M., Choi, Y.-J., Kowalski, R. A., Larson, S., Warner, B. D., Marshalkina, A. L., Ibrahimov, M. A., Molotov, I. E., Michałowski, T., Kitazato, K., 2008b. New photometric observations of asteroids (1862) Apollo and (25143) Itokawa - an analysis of YORP effect. *Astron. Astrophys.* 488, 345–350.
- Gaskell, R., Saito, J., Ishiguro, M., Kubota, T., Hashimoto, T., Hirata, N., Abe, S., Barnouin-Jha, O. S., Scheeres, D., 2006. Global Topography of Asteroid 25143 Itokawa. In: Mackwell, S., Stansbery, E. (Eds.), 37th Annual Lunar and Planetary Science Conference. Vol. 37 of Lunar and Planetary Institute Conference Abstracts. pp. 1876–1877.
- Greenberg, R., Nolan, M. C., Bottke, Jr., W. F., Kolvoord, R. A., Veverka, J., 1994. Collisional history of Gaspra. *Icarus* 107, 84–97.
- Hapke, B., 1984. Bidirectional reflectance spectroscopy. III - Correction for macroscopic roughness. *Icarus* 59, 41–59.
- Hapke, B., 2002. Bidirectional Reflectance Spectroscopy. 5. The Coherent Backscatter Opposition Effect and Anisotropic Scattering. *Icarus* 157, 523–534.
- Harris, A. W., Fahnestock, E. G., Pravec, P., Feb. 2009. On the shapes and spins of “rubble pile” asteroids. *Icarus* 199, 310–318.
- Helfenstein, P., Veverka, J., 1989. Physical characterization of asteroid surfaces from photometric analysis. In: Binzel, R. P., Gehrels, T., Matthews, M. S. (Eds.), *Asteroids II*. pp. 557–593.
- Holsapple, K. A., 2007. Spin limits of Solar System bodies: From the small fast-rotators to 2003 EL61. *Icarus* 187, 500–509.
- Housen, K. R., Holsapple, K. A., 2003. Impact cratering on porous asteroids. *Icarus* 163 (1), 102–119.
- Kaasalainen, M., 2004. Physical models of large number of asteroids from calibrated photometry sparse in time. *Astron. Astrophys.* 422, L39–L42.
- Kaasalainen, M., Kwiatkowski, T., Abe, M., Piironen, J., Nakamura, T., Ohba, Y., Dermawan, B., Farnham, T., Colas, F., Lowry, S., Weissman, P., Whiteley, R. J., Tholen, D. J., Larson, S. M., Yoshikawa, M., Toth, I., Velichko, F. P., 2003. CCD photometry and model of MUSES-C target (25143) 1998 SF36. *Astron. Astrophys.* 405, L29–L32.
- Kaasalainen, M., Lamberg, L., Lumme, K., Bowell, E., 1992. Interpretation of lightcurves of atmosphereless bodies. I - General theory and new inversion schemes. *Astron. Astrophys.* 259, 318–332.
- Kaasalainen, M., Torppa, J., 2001. Optimization Methods for Asteroid Lightcurve Inversion. I. Shape Determination. *Icarus* 153, 24–36.
- Kaasalainen, M., Đurech, J., Warner, B. D., Krugly, Y. N., Gaftonyuk, N. M., 2007. Acceleration of the rotation of asteroid 1862 Apollo by radiation torques. *Nature* 446, 420–422.
- Lagerros, J. S. V., 1996. Thermal physics of asteroids. I. Effects of shape, heat conduction and beaming. *Astron. Astrophys.* 310, 1011–1020.
- Lamy, P. L., Kaasalainen, M., Lowry, S., Weissman, P., Barucci, M. A., Carvano, J., Choi, Y.-J., Colas, F., Fauray, G., Fornasier, S., Groussin, O., Hicks, M. D., Jorda, L., Kryszczyńska, A., Larson, S., Toth, I., Warner, B., 2008. Asteroid 2867 steins. *Astronomy and Astrophysics* 487 (3), 1179–1185.
- Lowry, S. C., Fitzsimmons, A., Pravec, P., Vokrouhlický, D., Boehnhardt, H., Taylor, P. A., Margot, J.-L., Galád, A., Irwin, M., Irwin, J., Kusnirák, P., 2007. Direct Detection of the Asteroidal YORP Effect. *Science* 316, 272–.
- Micheli, M., Paolicchi, P., 2008. YORP effect on real objects. I. Statistical properties. *Astron. Astrophys.* 490, 387–391.
- Muñón, K., Lagerros, J. S. V., 1998. Inversion of shape statistics for small solar system bodies. *Astron. Astrophys.* 333, 753–761.
- Mysen, E., 2008a. An analytical model for YORP and Yarkovsky effects with a physical thermal lag. *Astron. Astrophys.* 484, 563–573.
- Mysen, E., 2008b. Dynamical effects of thermal emission on asteroids. *Mon. Not. R. Astron. Soc.* 383, L50–L53.
- Nakamura, A. M., 2002. Cratering of asteroids and small bodies. *Advances in Space Research* 29 (8), 1221–1230.
- Nesvorný, D., Vokrouhlický, D., 2007. Analytic theory of the yorp effect for near-spherical objects. *The Astronomical Journal* 134 (5), 1750–1768.
- Nesvorný, D., Vokrouhlický, D., 2008. Analytic theory for the yarkovsky-okeefe-radzievski-paddack effect on obliquity. *The Astronomical Journal* 136 (1), 291–299.
- Nesvorný, D., Vokrouhlický, D., 2008. Vanishing torque from radiation pressure. *Astron. Astrophys.* 480, 1–3.
- O'Brien, D. P., Greenberg, R., Richardson, J. E., 2006. Craters on asteroids: Reconciling diverse impact records with a common impacting population. *Icarus* 183 (1), 79–92.
- Ostro, S. J., Benner, L. A. M., Nolan, M. C., Magri, C., Giorgini, J. D., Scheeres, D. J., Broschart, S. B., Kaasalainen, M., Vokrouhlický, D., Chesley, S. R., Margot, J.-L., Jurgens, R. F., Rose, R., Yeomans, D. K., Suzuki, S., de Jong, E. M., 2004. Radar observations of asteroid 25143 Itokawa (1998 SF36). *Meteoritics and Planetary Science* 39, 407–424.
- Rubincam, D. P., 2000. Radiative Spin-up and Spin-down of Small Asteroids. *Icarus* 148, 2–11.
- Saito, J., Miyamoto, H., Nakamura, R., Ishiguro, M., Michikami, T., Nakamura, A. M., Demura, H., Sasaki, S., Hirata, N., Honda, C., Yamamoto, A., Yokota, Y., Fuse, T., Yoshida, F., Tholen, D. J., Gaskell, R. W., Hashimoto, T., Kubota, T., Higuchi, Y., Nakamura, T., Smith, P., Hiraoka,

- K., Honda, T., Kobayashi, S., Furuya, M., Matsumoto, N., Nemoto, E., Yukishita, A., Kitazato, K., Dermawan, B., Sogame, A., Terazono, J., Shinohara, C., Akiyama, H., 2006. Detailed Images of Asteroid 25143 Itokawa from Hayabusa. *Science* 312, 1341–1344.
- Scheeres, D. J., 2007a. Rotational fission of contact binary asteroids. *Icarus* 189, 370–385.
- Scheeres, D. J., 2007b. The dynamical evolution of uniformly rotating asteroids subject to YORP. *Icarus* 188, 430–450.
- Scheeres, D. J., Abe, M., Yoshikawa, M., Nakamura, R., Gaskell, R. W., Abell, P. A., 2007. The effect of YORP on Itokawa. *Icarus* 188, 425–429.
- Scheeres, D. J., Gaskell, R. W., 2008. Effect of density inhomogeneity on yorp: The case of itokawa. *Icarus* 198 (1), 125–129.
- Slivan, S. M., Sep. 2002. Spin vector alignment of Koronis family asteroids. *Nature* 419, 49–51.
- Taylor, P. A., Margot, J.-L., Vokrouhlický, D., Scheeres, D. J., Pravec, P., Lowry, S. C., Fitzsimmons, A., Nolan, M. C., Ostro, S. J., Benner, L. A. M., Giorgini, J. D., Magri, C., 2007. Spin Rate of Asteroid (54509) 2000 PH5 Increasing Due to the YORP Effect. *Science* 316, 274–277.
- Thomas, P. C., Joseph, J., Carcich, B., Veverka, J., Clark, B. E., Bell, J. F., Byrd, A. W., Chomko, R., Robinson, M., Murchie, S., Prockter, L., Cheng, A., Izenberg, N., Malin, M., Chapman, C., McFadden, L. A., Kirk, R., Gaffey, M., Lucey, P. G., 2002. Eros: Shape, topography, and slope processes. *Icarus* 155 (1), 18–37.
- Thomas, P. C., Veverka, J., Bell, J. F., Clark, B. E., Carcich, B., Joseph, J., Robinson, M., McFadden, L. A., Malin, M. C., Chapman, C. R., Merline, W., Murchie, S., 1999. Mathilde: Size, shape, and geology. *Icarus* 140 (1), 17–27.
- Veverka, J., Thomas, P. C., Robinson, M., Murchie, S., Chapman, C., Bell, M., Harch, A., Merline, W. J., Bell, J. F., I., Bussey, B., Carcich, B., Cheng, A., Clark, B., Domingue, D., Dunham, D., Farquhar, R., Gaffey, M. J., Hawkins, E., Izenberg, N., Joseph, J., Kirk, R., Li, H., Lucey, P., Malin, M., McFadden, L., Miller, J. K., Owen, W. M., J., Peterson, C., Prockter, L., Warren, J., Wellnitz, D., Williams, B. G., Yeomans, D. K., 2001. Imaging of Small-Scale Features on 433 Eros from NEAR: Evidence for a Complex Regolith. *Science* 292 (5516), 484–488.
- Vokrouhlický, D., Čapek, D., 2002. YORP-Induced Long-Term Evolution of the Spin State of Small Asteroids and Meteoroids: Rubincam's Approximation. *Icarus* 159, 449–467.
- Vokrouhlický, D., Čapek, D., Kaasalainen, M., Ostro, S. J., 2004. Detectability of YORP rotational slowing of asteroid 25143 Itokawa. *Astron. Astrophys.* 414, L21–L24.
- Walsh, K. J., Richardson, D. C., Michel, P., 2008. Rotational breakup as the origin of small binary asteroids. *Nature* 454, 188–191.